Numerical Analysis of RPM effect on Dynamic Stall Phenomena on Helicopter Rotor at High Thrust Forward Flight

Camille Castells, François Richez, Michel Costes

Numerical Analysis of RPM effect on Dynamic Stall Phenomena on Helicopter Rotor at High Thrust Forward Flight

Camille Castells
PhD Student
ONERA, The French Aerospace Lab
Meudon, France

François Richez
Research Scientist
ONERA, The French Aerospace Lab
Meudon, France

Michel Costes
Research Scientist
ONERA, The French Aerospace Lab
Meudon, France

ABSTRACT

Dynamic stall is a highly complex phenomenon characterized by unsteady massive separated flow. It limits the flight envelope of helicopters by generating vibrations and large dynamic loads which can lead to fatigue and structural failure of blades. Dynamic stall involves several mechanisms which make the numerical prediction of stall difficult and the understanding of the phenomenon still incomplete. A loose coupling methodology between a Computational Fluid Dynamics and a Comprehensive Analysis codes is used to simulate the problem. Three stalled flight conditions have been selected in the wind tunnel 7A rotor test data to investigate the RPM effect on the dynamic stall onset and the related mechanisms. The lower the RPM, the more severe the stall is. A double stall has been observed on the lowest RPM case. The coupled simulations are in satisfactory agreement with experiment and are used to identify the mechanisms leading to stall. Simulations indicate that the blade-vortex interaction is an important factor in triggering the different stall events in these configurations.

NOTATION

HRPM	High RPM
LRPM	Low RPM
MRPM	Moderate RPM
LE	Leading Edge
TE	Trailing Edge
R	Rotor Radius, m
c	Blade chord,m
Ω	Rotational speed, rpm
M_{tip}	Tip Mach number
μ	Advance Ratio
C_L/σ	Rotor Lift coefficient
C_X/σ	Rotor Propulsive force coefficient
M^2C_n	Section normal force
M^2C_m	Section pitching moment
α_t	Shaft angle, deg
θ_0	Collective pitch angle, deg
$\theta_1 c$	Lateral cyclic pitch angle, deg
$\theta_1 s$	Longitudinal cyclic pitch angle, deg
ψ	Blade azimuthal position,deg
σ	Rotor solidity
K_p	Pressure coefficient
$K_{p,crit}$	Critical pressure coefficient where the local Mach number is one
x_{sep}/c	Chordwise position of flow separation point
l_{sep}/c	Chordwise length of flow separation region

Presented at the Vertical Flight Society 75th Annual Forum & Technology Display, Philadelphia, Pennsylvania, May 13–16, 2019.

INTRODUCTION

Dynamic stall is one of the most limiting phenomena occurring during helicopter operation, especially in forward flight or in maneuvers. In these flight conditions, a dissymetry of airspeed is observed on the rotor disk due to the combination of rotating and advancing speed with respect to the azimuthal position of the blade. To balance the rotor loads and remove the corresponding rolling motion, the angle of attack has to be periodically modified. It is reduced on the advancing side where the airspeed is higher and it is increased on the retreating side where the velocity is lower. For the most severe flight conditions, the local angle of attack on blade sections exceeds the static stall angle and reaches a critical angle of attack. Beyond this angle, the boundary layer massively separates, the lift is considerably decreased and a strong negative pitching moment is observed. This phenomenon occurring at each rotor revolution causes vibrations, loss of the aircraft controls and eventually damages to the blade structure. It is called dynamic stall (Ref. 1).

Dynamic stall is still one of the most studied phenomena experienced by helicopter rotors since new rotorcraft are expected to operate with higher speed and thrust. However, it remains a challenging phenomenon of the rotorcraft environment for numerical prediction since it involves several mechanisms which are not well understood and challenging to predict. One can

name three-dimensional unsteady separated flow, transonic flow including shocks, reverse flow, blade-vortex interaction, vortex shedding or fluid-structure coupling.

A renewed interest on the problem could be noted over the last twenty years thanks to the progress of CFD in dealing with viscous separated flows, progressively switching from simplified cases to more realistic ones.

Until very recently, most studies dedicated to dynamic stall were carried out on simplified configurations, typically two-dimensional airfoils in oscillating pitching motion simulating the evolution of the angle of attack during a rotor revolution (Ref. 2). Experimental (Refs. 2, 3) and numerical (Refs. 4, 5) studies allowed scientists to investigate and obtain a better understanding of the different mechanisms occurring during a dynamic stall event. It highlighted the hysteresis aspect of the lift and the pitching moment. It also brought out that the sharp decrease in pitching moment is observed before the decrease in lift. It is explained by the shedding of the dynamic stall vortex travelling downstream from leading edge to trailing edge. Two-dimensional simulations allowed the determination of the numerical requirements needed to capture dynamic stall events for a reduced time-cost. One can mention the work of Refs. 5 and 6 on the time and space resolution, the work of Srinivasan *et al.* (Ref. 7) on turbulence modelling or the investigations carried out on the influence of the prediction of boundary layer transition on stall (Refs. 8, 9). Reference 10 also highlighted that two-dimensional numerical simulations cause an earlier onset of the stall event, overpredict the separation and delay the reattachment with respect to similar three-dimensional configurations.

Then, three-dimensional configurations were investigated to take into account the influence of the finite span character of the blade and the impact of the tip vortex on stall onset. Le Pape *et al.* showed experimentally on a OA209 wing that three-dimensional mechanisms are present during a stall event (Ref. 11). The tip vortex of the wing produces a downward flow which tends to delay the stall onset. Thus, the flow separation occurs at the inner part of the wing and then spreads to the tip where the tip vortex delays flow separation. Numerical studies (Refs. 12–14) used Ref. 11 to validate the CFD methods and to provide the best set of numerical parameters and physical models for stall prediction.

The next step in the dynamic stall studies is the inclusion of the blade rotation. Schwermer *et al.* (Ref. 15) established an experimental set-up to investigate a rotating blade in pitching oscillation motion. The effect of rotation is to keep the stall vortex closer to the blade surface with respect to a non rotating configuration which was also observed numerically by Gardner and Richter (Ref. 16).

In realistic rotor environment, the dynamic stall mechanisms are expected to be quite different from the isolated wing since blade-wake interaction or blade articulation and deformation can influence the stall onset by modifying locally the angle of attack. Bousman (Ref. 17) was the first to investigate the dynamic stall in complete rotor environment on three conditions extracted from flight tests of the UH-60A Black Hawk helicopter (Ref. 18): two maneuvers and one stalled forward flight. Potsdam *et al.* (Ref. 19) developed a fluid/structure coupling strategy between a Comprehensive Analysis (CA) code and a Computational Fluid Dynamics (CFD) solver. Three flight conditions from Ref. 18 including the stalled forward flight studied by Bousman were computed. The coupling computation gave a good agreement with respect to the experimental data available. Ortun et al. (Ref. 20) also validated the CFD/CA coupled simulation on 7A rotor configurations. Richez et al. (Ref. 21) provided the numerical requirements necessary to predict stall at high thrust forward flight. Recent works (Refs. 20–23) on different stalled flight conditions highlights the capability of numerical tools to predict dynamic stall on rotor configurations. They provide some clues on the several mechanisms involved in the stall onset such as blade-vortex interaction in a high angle of attack area (Refs. 23, 24) or the torsional response of the blade (Ref. 24).

The objective of the present work is to get a better understanding of the mechanisms occurring during stall events in rotor environment, especially the influence of the RPM on stall onset and strength. Three flight conditions with potentially different stall mechanisms are compared using coupled CFD/CA simulations.

EXPERIMENTAL DATABASE

A wide range of flight conditions of the model-scale 7A rotor, represented in Fig. 1, have been tested in the transonic closed circuit S1MA wind tunnel at ONERA Modane test center, France, in 1991 (Ref. 25). The 7A rotor, of radius R=2.1m, is composed of four articulated blades of constant chord c = 0.14 m and constant twist rate of -8.3 deg/R. The blade is made of two airfoils. The 13% relative thickness OA213 airfoil is used from inboard to 0.75R and the 9% relative thickness OA209, from 90% of the rotor radius to the tip. An extensive database is available including high thrust and high speed cases. It provides unsteady pressure measurements, integrated section normal forces and pitching moments at the five blade radial stations r/R = 0.5, 0.7, 0.825, 0.915, and 0.975 as well as blade bending moments and motion (rigid angles and elastic deformations).

Three configurations have been selected in the database for the numerical investigation presented in this work. They reflect the influence of the rotor angular speed on the dynamic stall mechanisms. All selected conditions have the same propulsive and lift forces. Table 1 summarizes the flow parameters for each flight condition investigated.

The decrease in RPM increases the dissymetry of velocity on the rotor disk. Thus, to maintain a trimmed rotor state, an increase of the angle of attack is necessary when the RPM is decreased. An increase of the pitch angle and of the flapping amplitude (Modane law : $\beta_{1c} = \theta_{1s}$) is actually obtained (Table 1). It results in an amplification of the stall event when the RPM is decreased. Dynamic stall is characterized by a severe loss of lift and a sharp negative pitching moment on the retreating blade, for $180\,\text{deg} \leq \psi \leq 360\,\text{deg}$. Figure 2 represents the phase-averaged evolution of the normal force

	Low RPM (LRPM)	Moderate RPM (MRPM)	High RPM (HRPM)
Ω, rpm	964	1022	1063
M_{tip}	0.616	0.646	0.676
μ	0.315	0.3	0.288
C_L/σ	0.09	0.1	0.11
C_X/σ	0.0044	0.0046	0.0049
α_t, deg	-6.75	-6.7	-6.45
θ_0, deg	9.7	8.4	7.2
$\theta_1 c$, deg	3.6	3.15	2.5
$\theta_1 s$, deg	-4.4	-3.5	-3.05

Table 1: Selected Flight Conditions

coefficient of the five instrumented sections. Lift stall events are clearly observed for the three cases at the outer sections, $r/R > 0.8$ for $270\,\text{deg} \leq \psi \leq 330\,\text{deg}$. Figure 3 illustrates the pitching moment coefficient for the available sections. The strong negative pitching moment at stall (M^2Cm steep negative peak) can be seen on the retreating blade, around 270 deg at the $r/R = 0.915$ section, for all the selected flight conditions. The reduction of RPM leads to an earlier stall onset due to higher angles of attack. For the highest rotational speed (HRPM), stall appears at the $r/R = 0.915$ section only at an azimuthal position of 280 deg while it starts at 240 deg for the lowest RPM tested (LRPM). One can also notice that for the most critical case (LRPM), a second strong stall event occurs at 330 deg for the $r/R = 0.915$ section which is not seen in the other cases. Experimental data are not available for the High RPM case at $r/R = 0.7$ section due to pressure sensors failure. Thus, this section will not be presented in the paper.

The objective of the present work is to get an understanding of the mechanisms occurring during these stall events by using numerical simulations.

COMPUTATIONAL METHODOLOGY

This work uses a loose coupling strategy between Computational Fluid Dynamics (CFD) and Comprehensive Analysis (CA), similarly to the work presented by Potsdam (Ref. 19).

The CFD part of the coupling procedure is performed with the unsteady Reynolds-Averaged Navier-Stokes (URANS) finite volume *elsA* (ONERA-Airbus-Safran property) solver developed by ONERA (Ref. 26). A Chimera approach is used, with near body curvilinear structured grids around each blade and around the experimental test stand, and background Cartesian grids (Fig. 4). The blade near body grid is composed of 5.7 million points (Table 2). The k-ω Kok SST turbulence model is chosen because it has shown a good capability to predict flow separation in previous work (Ref. 27). The time derivative is discretized with a second order implicit Gear scheme. At each time step, the non-linear problem is solved by an iterative Newton process. The time step is set to $\Delta\psi = 0.225$ deg with 30 sub-iterations in the Newton iterative process in order to get second-order time-accurracy (Ref. 28). The time step used in the following results has been validated for the test case at the moderate RPM flight condition (MRPM). It gives a solution which is weakly dependent with respect to the time resolution during the stall event.

Blade mesh size	5.7M
y^+	0.6
Boundary Layer points	35-50
Chordwise points	313
Radial points	155
Normal points	61
Leading Edge Spacing	0.1%c
Finest Cartesian grid Spacing	$< 10\%$c

Table 2: Mesh Specification

The HOST comprehensive analysis code from Airbus Helicopters (Ref. 29) is used to take into account the blade motion and deformation in the coupled simulations. It is based on the lifting line theory for aerodynamics and beam theory with modal decomposition to describe the blade structure. Seven modes and seven harmonics have been used to characterize the blade deformation. The aerodynamic loads provided by the CFD solver are used by the comprehensive code to compute the trim control angles and also the kinematics and deformations of the blades, which are, then, used by *elsA* to prescribe the motion and deformation of the blade grids. The coupling between codes is made at each rotor revolution. The simulations are stopped when the rotor control angles and the airloads reach an equilibrium state. For the present computations, such a convergence typically requires 10 to 15 revolutions.

VALIDATION

The converged trim control angles obtained by the coupling process are compared to the experimental data available for each flight condition. The numerical calculations are in good agreement with the wind tunnel results as shown in Table 3.

	LRPM	MRPM	HRPM
Experiment: α_t, deg	-6.75	-6.7	-6.45
elsA/HOST: α_t, deg	-6.44	-6.4	-6.1
Experiment: θ_0, deg	9.7	8.4	7.2
elsA/HOST: θ_0, deg	9.7	8.6	7.2
Experiment: $\theta_1 c$, deg	3.6	3.15	2.5
elsA/HOST: $\theta_1 c$, deg	3.9	3.36	2.8
Experiment: $\theta_1 s$, deg	-4.4	-3.5	-3.05
elsA/HOST: $\theta_1 s$, deg	-4.4	-3.7	-3.01

Table 3: Trim Control Angles Comparison for each flight case

The trim angles are well estimated by the coupling method with a difference of less than 0.3 deg with experiment for

all control angles. The test-stand used during the experiment has been taken into account in the computation (Fig. 4) since Ortun (Ref. 20) shows that it improves the lateral cyclic pitch angle estimation of the simulation by deflecting the flow in the rotor disk and so modifying the local angle of attack. The test-stand creates an upwash flow on the front of the rotor, $\psi = 180\,\text{deg}$, and a downwash flow on the rear part, $\psi = 0\,\text{deg}$, thus inducing a decrease of the local angle of attack at $\psi = 0\,\text{deg}$ and an increase at $\psi = 180\,\text{deg}$ which is directly balanced by the lateral pitch angle.

The sectional normal force and pitching moment coefficients (respectively M^2C_n and M^2C_m), which are available in the experimental database, are compared to the computed results in Figure 5 to 10. In order to avoid a systematic error to get these quantities from *elsA*, the same integration procedure applied in the tests was used by interpolating the computed pressure at the location of the unsteady pressure transducers.

For the moderate RPM test case, the dynamic stall event is captured by the simulation. The decrease of M^2C_n and M^2C_m are well predicted by the coupled calculations (Figs. 9 and 6). The mimimum of M^2C_n, obtained at $\psi = 300\,\text{deg}$ for the $r/R = 0.915$ section, is slightly overestimated but the stall event is well predicted in amplitude and in phase. The pitching moment coefficient is more sensitive and more difficult to capture, but the agreement between simulations and experiments is satisfactory since the moment stall occurs at the right azimuthal position. The minimum of M^2C_m is reached at $\psi = 290\,\text{deg}$ for the $r/R = 0.915$ section. One can notice that the minimum value reached is underestimated (more negative) by the CFD/CA computation. A second small variation of M^2Cm, which is visible but less intense in the experimental data, is predicted by simulation for $r/R = 0.915$, $\psi = 330\,\text{deg}$. It is probably due to the slight overestimation of the pitch angle and of the shaft.

For the high RPM case, the stall observed is weaker than the one observed in the MRPM case (Fig. 3). Figure 5 shows that the sectional normal force coefficients are well captured by the calculation. However, one can notice, in Figure 8, that the negative pitching moment peak induced by stall is almost missed by the simulation. A slight decrease in the pitching moment is indeed observed at stall position $\psi = 290\,\text{deg}$ for $r/R = 0.915$ but it is strongly underestimated with respect to the experimental data. This kind of behaviour has already been observed in two-dimensional configurations. Light stalls where the pitching angle oscillations remain close to the stall angle are more difficult to capture by numerical simulations.

The two dynamic stall events observed for a lower RPM are captured with a good agreement with experimental results (Figs. 7 - 10). Both of the events are however overestimated (more severe) in terms of pitching moment coefficient but are well captured in terms of azimuthal phase of the stall onset, the first stall event starting at $\psi = 240\,\text{deg}$ and the second one at $330\,\text{deg}$ at the section $r/R = 0.915$ (Fig. 10). Therefore it can be concluded that the loose coupling method correctly captures dynamic stall events for these three different flight configurations.

Besides the airloads, the coupled procedure shows a good capability to predict the structural loads of the rotor blades. Figure 11 depicts the evolution of the torsional moments obtained by the CA/CFD with respect to the experiment. Two sections ($r/R = 0.3$ and $r/R = 0.65$) of the blade are represented. The computations are in good agreement bwith the experiments. The 5/rev frequency content of the torsional moment is well predicted by the *elsA*/HOST computations for all cases. The amplitude are overestimated in the MRPM and the LRPM cases but the azimuthal phase correlation between the simulation and the experimental data is satisfactory for the two sections considered.

ANALYSIS

Description of the separated flow regions

It was shown above that the numerical results are in good agreement with the experimental data in these three stalled configurations. Thus, it was concluded that the simulation correctly captures the mechanisms of the stall events and is representative of the phenomenon investigated. The numerical results are used to identify the stall regions and their features during these flight conditions. Rotormaps of the chordwise flow separation point position x_{sep} and chordwise flow separation length l_{sep} at each radial section and azimuthal step have been established. The separation point, x_{sep}, is defined as the point where the tangential component of the friction vector becomes negative and, in the same way, the reattachment point is reached when it becomes positive again. The tangential unit vector is defined as shown in Fig. 12. The leading edge is the origin of the local chordwise axis so $x/c = 0$ represents the leading edge (LE) position while $x/c = 1$ is the trailing edge (TE). Thus, $x_{sep}/c = 0$ defines a flow separation at the very leading edge while $x_{sep}/c = 1$ means that there is no flow separation. In the same way, the chordwise length l_{sep} of the flow separation at each radial and azimuthal position is computed and $l_{sep}/c = 0$ means that no flow separation is detected while $l_{sep}/c \approx 1$ defines a fully separated flow along the chord.

Castillo et al. proposed, in Ref. 30, a boundary layer separation criterion based on the shape factor: $H_{sep} = 2.76$. This criterion has been validated on experimental results. However, this criterion is not able to detect clearly the reattachment and thus the separation flow length in these configurations. The criterion based on the friction lines, used to detect flow separation features has been validated by comparison with the one based on the shape factor used by Richez in Ref. 21. Figure 13 shows that the two different strategies of flow separation detections predict similar separation regions. The postprocessing tool used by Richez in Ref. 21 filtered some flow separation regions notably the small bubbles near the stagnation point, thus explaining the differences noticeable in Fig. 13.

The rotormaps of the chordwise flow separation point position computed for the studied configurations are presented in Figure 14 and rotormaps of the chordwise flow separation length

is illustrated in Figure 15. They reveal four flow separation regions for all cases. They are circled in black. They also exhibit an increase of the global separated flow area on the rotor disk with the decrease in RPM. The reverse flow region is a region close to the retreating blade root where the flow is coming from the trailing edge to the leading edge. From the definition of the separation criterion based on the friction lines, the reverse flow is detected as a boundary layer separation but it will not be considered in the following discussion.

The first flow separation occurring on the blade is located on the inner part of the blade ($0.4 \leq r/R \leq 0.8$) in the third quadrant of the rotor disk, $180 \leq \psi \leq 270$. This region is referred to as "A" in Figures 14 and 15. The boundary layer separates at the trailing edge at $r/R = 0.6$, $\psi = 150\,\text{deg}$ and moves towards the leading edge when the blade pursues its revolution. Figure 14 also highlights that the flow separation moves further upstream when the RPM is decreased. Thus, the flow separation point does not reach further than the quarter of chord in the high RPM case, $x_{sep}/c = 0.3$ at $\psi = 250\,\text{deg}$. In contrast, it reaches the leading edge, $x_{sep}/c \approx 0$, for the two lower RPM cases and at an increasingly early azimuthal position of the blade. For the $r/R = 0.5$ section, the separation point reached the leading edge at $\psi = 240\,\text{deg}$ for the moderate RPM case and at $\psi = 225\,\text{deg}$ for the lowest RPM case. The separation also spreads radially, contaminating more external sections of the blade. Figure 15 shows that, for the two lowest RPMs cases, this region leads to a massive flow separation ($l_{sep}/c \geq 0.9$) which is responsible of the stall events observed in Fig. 5 - 10, at $r/R = 0.5$, while no stall is observed in the HRPM case in this section.

A second flow separation region occurs at the blade tip for $210\,\text{deg} \leq \psi \leq 310\,\text{deg}$ and is referred to as "B" in Figures 14 and 15. Firstly for $\psi \leq 270\,\text{deg}$, the separation suddenly appears on the leading edge of the blade and immediately reattaches as illustrated in Figure 15, the separation flow length being less than 5% of the blade chord. However, as the blade reaches a critical azimuthal position, the bubble bursts for the two lowest RPM cases. Figure 15 exhibits the massive flow separation ($l_{sep}/c \approx 1$) leading to the stall events seen on these two cases at the tip region of the blade in Fig. 5 - 10. It occurs at $\psi = 290\,\text{deg}$ on MRPM and at $\psi = 270\,\text{deg}$ on LRPM. The bubble does not burst in the high RPM case since the flow separation remains smaller than 10% of the blade chord.

The next flow separation area, referred to as C, is located at the end of the fourth quadrant ($330\,\text{deg} \leq \psi \leq 360\,\text{deg}$) also at the blade tip region (Fig. 14-15). For all the cases, the boundary layer first separates and immediately reattaches leading to a small separation bubble. As the azimuth increases, the bubble expands and gives a massive flow separation only for the LRPM test case. This flow separation leads to the second stall event observed on the airloads in Fig. 7 and 10. For the moderate RPM case, the separated flow reaches 30% of the blade chord which explains the small pitching moment fluctuations seen in Fig. 9, at $r/R > 0.915$ and $\psi = 330\,\text{deg}$. For the HRPM case, the separation bubble of region B (Fig. 14) does not reach a length sufficient to influence the loads since $l_{sep}/c < 5\%$ (Fig. 15).

The Flow Separation region D (Fig. 14-15) appears on the advancing side ($0\,\text{deg} \leq \psi \leq 90\,\text{deg}$) in the tip region of the blade. This flow separation does not reach a size which can lead to stall. For all cases, Figure 15 shows that $l_{sep}/c < 10\%c$ in region D. A second flow separation occurs in the region D in the LRPM test case. It appears at blade tip in the same region of the rotor disk, in the first quadrant.

Analysis of Flow Separation in Region A

In Reference 31, Droandi et al. showed experimentally and numerically that the incidence induced by the passage of a perpendicular vortex close to a NACA 23012 airfoil causes a flow separation onset leading to stall. Richez (Ref. 24) highlighted that the blade-vortex interaction also triggers the dynamic stall onset on realistic configurations of helicopter rotor. In the studied rotor configurations, the vortex is not always perpendicular to the blade when the interaction takes place which is quite different from what was already investigated in two-dimensional configurations (Refs. 31, 32). The flight condition investigated in Ref. 24 corresponds the moderate RPM case considered in the present work.

In this section, the effect of the BVI on stall event of region A is investigated for each rotor configuration. An analytical tool is implemented to estimate the location of the interaction between a blade and the tip vortex of the preceding blades. To do so, an analytical prediction of the position of the tip vortices emitted is computed. A helicoidal shape of the vortex driven by the rotational velocity of the rotor and the translational speed of the aircraft is assumed. The lead-lag and flap motions of the blade are considered in the computation as well as the shaft angle. The radial position of the interaction with the blade can then be easily determined. For clarification purposes, a snapshop of the analytical vortices for a blade at $\psi = 280\,\text{deg}$ for the MRPM case is shown in Figure 16. A good agreement between the isocontour of Q criterion computed from the *elsA*/HOST simulation and the analytical vortices can be noted. The intersection point between the blade and the tip vortex paths at the retreating blade is cercled in black in Fig. 16.

The radial position of the intersection of the blade with the helicoidal vortices has been computed for each azimuth. These intersection lines are represented with black lines overlayed on the rotormaps of the chordwise flow separation point in Figure 17 and on the rotormaps of the chordwise flow separation length in Figure 18. For all cases, it is clear that the blade-vortex interaction and the separation flow development are linked, especially in region A.

The interaction occurring in region A has started at the tip of the blade at the azimuth $\psi = 90\,\text{deg}$, when the blade is set at a low angle of attack. Thus, the vortex passage does not induce a sufficient rise of angle of attack to trigger boundary layer separation. When the blade goes on with its revolution, the pitch angle is increased and the vortex influence becomes more critical. A flow separation begins to develop from the trailing edge at $r/R = 0.6$ at the interaction point for

$\psi \approx 180$ deg and moves towards the leading edge as ψ and the angle of attack increase. The lower the RPM is, the earlier the stall occurs since the kinematic-induced angle of attack is higher when the RPM is decreased. Stall onset in region A is marked by a + for the two lower RPM cases in Fig. 17 and 18. For the HRPM test case, the sign + shows the region where the flow separation length reaches its maximum. Figure 19 illustrates the isocontour of Q criterion for all the cases for a blade at the position marked by the + in Fig. 17 and 18. The dynamic stall vortex characterized by a high level of turbulent kinetic energy can be distinguished from tip vortices that are characterized by low level of turbulent kinetic energy. At such azimuthal position, the stall events observed in Fig. 5-10, at $r/R = 0.5$, start growing and can be identified in Fig. 19 by the high level of turbulent kinetic energy k. The stall develops at the blade-vortex interaction point and then, as ψ is increased, spreads radially around the BVI as illustrated in Fig. 17 and 18.

Analysis of Flow Separation in Region B

Figures 17 and 18 also show that the region B occurs in an area where the preceding blade tip vortex is close to the blade. A small separation bubble at the leading edge is observed before the BVI, for $\psi < 270$ deg for all cases in Fig. 17 and 18, but this separation length remains smaller than 10% of the blade chord. When the tip vortex comes closer to the blade, it seems to trigger the bubble bursting for the MRPM case. In this case, the sudden growth of the bubble size is occurring at the time of the interaction between the blade and the tip vortex ($\psi = 280$ deg). In Figures 17 and 18 the point marked by a $\circ$ represents the stall onset. It occurs at the azimuth of the blade-vortex interaction for the MRPM case. However, for the LRPM case, the stall onset is occurring before the blade-vortex interaction. In Figure 20, the isocontour of the Q criterion for a blade at the $\circ$ position is represented for all the cases, ie. at the stall onset for the two lower RPM cases and at the larger separation bubble for the HRPM case. At this position of the blade, the tip vortex is close to the blade tip where the stall vortex is growing, especially in the two lower RPM cases. The stall vortex on the blade surface is recognizable by the high level of turbulence energy. For the LRPM case, as observed in Fig. 17 and 18, the stall is triggered when the tip vortex is still far from the blade. Thus, the stall onset cannot in this case obviously be attributed to the blade-vortex interaction.

In this region, the mechanisms at the origin of stall appears to be more difficult to analyze than in the inner part of the blade (region A). To get a better understanding of the correlation between the motion of the blade and the stall events, further analysis of the phenomena occurring at the tip region of the blade is necessary. The azimuthal evolution of the pitch angle, the Mach number and the torsion angle at the $r/R = 0.915$ section are represented in Figures 22, 23 and 24 respectively for the HRPM, MRPM and LRPM cases. The sectional pitching moment coefficient and chordwise flow separation areas are also illustrated in these figures in order to compare the azimuthal phase of the phenomena. In order to facilitate the reading, the flow separation regions B, C and D observed at the blade tip in Fig. 14 and 15 are grayed.

In Figure 24, the pitch angle is found to be higherfor the LRPM case than the two other cases (Fig. 22-23). It reaches 18 deg at the stall onset ($\psi = 260$). It is higher than the pitch angle obtained at the intersection point between the blade and the tip vortex leading to stall for the MRPM test case, $\theta < 17$ deg at $\psi = 270$. Thus, it can be assumed that the variation of the angle of attack induced by the tip vortex could be enough to trigger the stall in this case, even if the vortex is still distant from the blade.

In Fig. 22, 23 and 24, the stall onset in region B is clearly seen in MRPM and LRPM cases. The separation bubble bursts at $\psi = 270$ deg for MRPM and at $\psi = 260$ deg for LRPM leading to a strong negative pitching moment. This excites the blade torsion mode, as a local minimum of the torsion angle is reached directly after the stall event. For the HRPM (Fig. 22), the separation bubble does not burst, probably due to the lower pitch angle compared to the two other cases. Thus, it does not lead to stall. Therefore, the amplitude of the blade torsion variation is smaller than for the lower RPM cases.

Analysis of Flow Separation in Region C

The third flow separation area, C, located at the end of the fourth quadrant of the rotor disk, in Fig. 14 and 15 also concerns the blade tip section. The flow separation at $r/R = 0.915$ is represented in Figures 22, 23 and 24. At such azimuthal position, the pitch angle is still high. The blade undergoes a flapping down motion due to the Modane law which imposes $\beta_{1c} = \theta_{1s}$. Furthermore, the torsional deformation angle of the blade is at a local maximum . Thus, one can assume that both kinematic and deformation of the blade contribute to increase the angle of attack in region C. The process assumed through the rotormaps analysis 17 and 18 is very similar to the one observed in region B. A small leading edge separation bubble is predicted for all cases at the end of the fourth quadrant which bursts at the blade-vortex interaction for the lowest RPM cases. In Figure 21, the isocontours of the Q criterion for the blade at $\psi = 330$ deg, marked by a $\diamond$ in Fig. 17 and 18, are presented for all the cases. This azimuthal position has been chosen to evaluate the mechanisms involved in the load variations seen at the blade tip $r/R > 0.915$ in Fig. 8, 9 and 10. A new blade-vortex interaction takes place when the blade is at $\psi = 330$ deg. Indeed, in this azimuthal range, the blade encounters the tip vortex emitted by the previous blade half a revolution earlier interacting with the previous dynamic stall event (B) which was convected behind the rotor. The vorticity in the vortex impacted is higher in the LRPM case ($Vorticity \approx 350 - 400 s^{-2}$) than in HRPM case ($Vorticity \approx 250 - 300 s^{-1}$). It probably contributes to increase the vortex-induced angle of attack. Thus, itcan be concluded that the mechanisms triggering flow separation in region C is a combination of several phenomena. The blade-vortex interaction coupled with the positive torsion angle and the high pitch angle (Fig. 22, 23 and 24) probably leads to

this second stall event, observed in the sectional airloads (Fig. 5 - 10, $r/R = 0.915$ and $r/R = 0.975$).

Analysis of Flow Separation in Region D

Flow Separation D occurs in a high Mach number region. The local Mach number is increasing due to the helicopter speed which is added to the rotational velocity of the blade until it reaches its maximum at $\psi = 90\,\text{deg}$. The evolution of the local Mach number and the torsion angle at $r/R = 0.915$ is presented in Fig. 22 for the HRPM case, in Fig. 23 for the MRPM case and in Fig. 24 for the LRPM case.

A flow separation is observed in this region for all cases. It occurs earlier with a high RPM because the shock appears earlier due to a high Mach number coupled with relatively high angles of attack. Figures 22, 23 and 24 also illustrate the evolution of the chordwise position of supersonic areas at $r/R = 0.915$ section for the three test cases. $K_{p,crit}$ is the pressure coefficient corresponding to a local Mach number equal to one. Thus, supersonic regions are characterized by $K_p - K_{p,crit} < 0$. Figures 22, 23 and 24 also include the location of the separation and the reattachment points of the different flow separations previously described. In region D, the small separation bubbles appear at the root of the shock wave, defined as the recompression edge of supersonic regions.

Two events are observed in region D for the LRPM case. Each area also coincides perfectly with a positive torsion peak seen in Figure 24. In the first event, the torsion adds 2 deg to the local angle of attack of the blade, significantly higher than for the two other RPM (Fig. 22-23). This high torsion angle is probably induced by the second stall event in region C which excites the blade torsion mode. It surely promotes the flow separation in region D.

Separation flows occuring in region D does not lead to stall in these three configurations since sectional normal forces and pitching moments do not show strong variation in these azimuthal and radial positions.

CONCLUSION

Loose coupling simulations between CFD code *elsA* and CA code HOST have been carried out for three helicopter flight conditions undergoing stall events. They correspond to the same flight condition of the helicopter at high speed and high thrust, with three different main rotor RPM regimes. Numerical parameters and turbulence model have been selected following the best practices determined in prior studies on pitching wings and helicopter rotors in stall conditions. For all cases, the numerical simulations have shown satisfactory agreement with the experimental data with regard to trim parameters (less than 0.3 deg difference with experiment for all control angles), airloads and structural loads (dynamic stall events correctly predicted in magnitude and phase). Different stall events have been distinguished for each case. The stall intensity increases with the decrease in the RPM. A trailing edge stall is observed for all cases in the inner part of the blade. For the two highest RPM cases, the blade tip undergoes one stall event at the beginning of the fourth quadrant of the rotor disk while it sees a double stall in the fourth quadrant for the lowest RPM case. The mechanisms that lead to these different stall events have been deeply investigated in this work. The onset of stall has been associated to the impact of the tip vortex generated by the other blades. The trailing edge stall and the strong leading edge stall occurring at the blade tip are triggered by the angle of attack induced by the vortex passing close to the blade. Stall only occurs when the kinematic induced angle of attack added to the vortex induced angle of attack is high enough. The second stall event in the low RPM case is connected to a second blade-vortex interaction. It takes place when the blade meets the tip vortex coming from the previous blade. Further investigations will be necessary to determine the influence of the vortex features on the dynamic stall onset. It also appears that the torsional deformation of the blade is sensitive to stall events occurring on the rotor. The dynamic stall, generating periodic strong negative pitching moments, induces negative torsion angles. Thus, it excites the torsion mode and leads to positive torsion angle peaks in the first quadrant. It was shown that, for these flight conditions, these local torsion maximums are correlated to flow separations and, thus, to load variations.

Author contact: Camille Castells camille.castells@onera.fr

ACKNOWLEDGMENTS

Part of this research was supported by a DGA scholarship. The studies presented in this article is making use of the elsA-ONERA software, whose the co-owners are Airbus, Safran, and ONERA

REFERENCES

[1]W. J. Mccroskey, "The phenomenon of dynamic stall," *NASA TM 81264*, 1981.

[2]W. J. McCroskey, K. W. McAlister, L. Carr, and S. L. Pucci, "An experimental study of dynamic stall on advanced airfoil sections," *NASA TM 84245*, 1982.

[3]R. Piziali, "2D and 3D oscillating wing aerodynamics for a range of angles of attack including stall.," in *NASA TM 4632*, 1994.

[4]G. Pailhas, R. Houdeville, P. Barricau, A. Le Pape, A. Faubert, P. Loiret, and F. David, "Experimental investigation of dynamic stall.," in *31st European Rotorcraft Forum Florence, Italy*, 2005.

[5]K. Richter, A. Le Pape, T. Knopp, M. Costes, V. Gleize, and A. Gardner, "Improved two-dimensional dynamic stall prediction with structured and hybrid numerical methods," in *Journal of the American Helicopter Society*, vol. 56, 2011.

[6]J. Ekaterinaris and M. Platzer, "Computational prediction of airfoil dynamic stall," in *Progress in Aerospace Sciences*, 1998.

[7]G. Srinivasan, J. Ekaterinaris, and W. McCroskey, "Evaluation of turbulence models for unsteady flows of an oscillating airfoil," *Computers & Fluids*, vol. 24, no. 7, pp. 833 – 861, 1995.

[8]M. Costes, V. Gleize, A. Le Pape, and F. Richez, "Numerical investigation of laminar/turbulent transition effects on the dynamic stall of an oscillating airfoil," in *American Helicopter Society Conference*, 2008.

[9]K. Richter, S. Koch, A. Gardner, H. Mai, A. Klein, and C.-H. Rohardt, "Experimental investigation of unsteady transition on a pitching rotor blade airfoil," *Journal of the American Helicopter Society*, vol. 59, pp. 1–13, 09 2012.

[10]M. Costes, F. Richez, A. Le Pape, and R. Gavériaux, "Numerical investigation of three-dimensional effects during dynamic stall.," in *37th European Rotorcraft Forum*, 2011.

[11]A. Le Pape, G. Pailhas, F. David, and J.-M. Deluc, "Extensive wind tunnel tests measurements of dynamic stall phenomenon for the OA209 airfoil including 3d effects," in *33rd European Rotorcraft Forum*, vol. 1, pp. 320–335, 01 2007.

[12]M. Costes, F. Richez, A. Le Pape, and R. Gavériaux, "Numerical investigation of three-dimensional effects during dynamic stall," *Aerospace Science and Technology*, vol. 47, no. Supplement C, pp. 216 – 237, 2015.

[13]K. Kaufmann, M. Costes, F. Richez, A. D. Gardner, and A. L. Pape, "Numerical investigation of three-dimensional static and dynamic stall on a finite wing," *Journal of the American Helicopter Society*, vol. 60, no. 3, pp. 1–12, 2015.

[14]R. Jain, M. Smith, A. Le Pape, M. Costes, and F. Richez, "High-resolution CFD predictions for static and dynamic stall of a finite-span OA209 wing," in *72nd American Helicopter Society International Annual Forum and Technology Display, At West Palm Beach, FL*, 2016.

[15]T. Schwermer, A. Gardner, and M. Raffel, "Dynamic stall experiments on a rotor with high cyclic setting in axial inflow," in *73rd American Helicopter Society International Annual Forum and Technology Display*, 2017.

[16]A. Gardner and K. Richter, "Influence of rotation on dynamic stall," in *68th American Helicopter Society International Annual Forum and Technology Display*, 2012.

[17]W. G. Bousman, "A qualitative examination of dynamic stall from flight test data," *Journal of the American Helicopter Society*, vol. 43, 1998.

[18]R. Kufeld, D. L. Balough, J. L. Cross, K. F. Studebaker, C. D. Jennison, and W. G. Bousman, "Flight testing the uh-60a airloads aircraft," in *50th American Helicopter Society International Annual Forum and Technology Display, Washington, DC*, 1994.

[19]M. Potsdam, H. Yeo, and W. Johnson, "Rotor airloads prediction using loose aerodynamic structural coupling," in *Journal of Aircraft*, vol. 43, 02 2004.

[20]B.Ortun, M. Potsdam, H. Yeo, and K. V. Truong, "Rotor loads prediction on the ONERA 7A Rotor using loose fluid/structure coupling," in *Journal of the American Helicopter Society*, 2016.

[21]F. Richez, "Numerical analysis of dynamic stall for different helicopter rotor flight conditions," in *73rd American Helicopter Society Annual Forum*, 2017.

[22]A.Grubb, C. Castells, R. Jain, F. Richez, and M. Smith, "High fidelity CFD analyses of dynamic stall on a four-bladed fully articulated rotor system," *74th American Helicopter Society International Annual Forum and Technology Display, Arizona, USA, May 14-17, 2018*, 2018.

[23]N. M. Chaderjian, "Navier-stokes simulation of UH-60A rotor wake interaction using adaptive mesh refinement," in *73rd American Helicopter Society International Annual Forum and Technology Display*, 2017.

[24]F. Richez, "Analysis of dynamic stall mechanisms in helicopter rotor environment," in *Journal of the American Helicopter Society*, vol. 63, 04 2018.

[25]P. Crozier, "Recent improvements in rotor testing capabilities in the ONERA S1MA wind tunnel.," in *20th European rotorcraft forum*, 1994.

[26]L. Cambier, S. Heib, and S. Plot, "The ONERA elsA CFD software: input from research and feedback from industry," *Mechanics & Industry*, vol. 14, no. 3, pp. 159–174, 2013.

[27]J. C. Kok, "Resolving the dependence on freestream values for the k- ω turbulence model," in *AIAA Journal*, vol. 38, pp. 1292–1295, 07 2000.

[28]N. Liggett and M. Smith, "Temporal convergence criteria for time-accurate viscous simulations of separated flows," *Computers & Fluids*, vol. 66, pp. 140 – 156, 2012.

[29]B. Benoit, A.-M. Dequin, K. Kampa, W. Grnhagen, P.-M. Basset, and B. Gimonet, "HOST, a general helicopter simulation tool for germany and france," in *56th American Helicopter Society International Annual Forum and Technology Display, Virginia Beach, VA (US)*, 01 2000.

[30]L. Castillo, X. Wang, and W. K George, "Separation criterion for turbulent boundary layers via similarity analysis," *Journal of Fluids Engineering*, vol. 126, 2004.

[31]G. Droandi, G. Gibertini, and A. Zanotti, "Perpendicular bladevortex-interaction over an oscillating airfoil in light dynamic stall," *Journal of Fluids and Structures*, vol. 65, pp. 472–494, 07 2016.

[32]A. Zanotti, G. Gibertini, and A. Mencarelli, "Experimental investigation of perpendicular vortex interaction over an oscillating airfoil in dynamic stall conditions," in *39th European Rotorcraft Forum*, pp. 85–88, 2013.

Fig. 1: 7A rotor mounted in ONERA Modane S1MA Wind Tunnel.

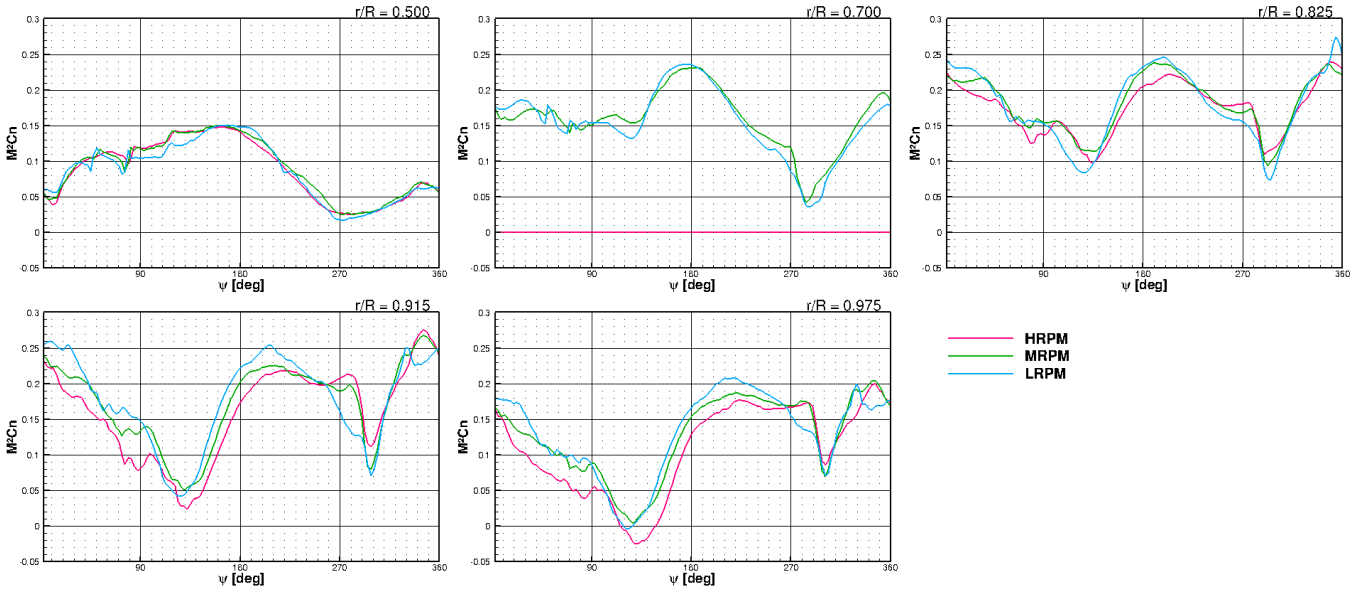

Fig. 2: Experimental sectional normal force coefficient M^2C_n.

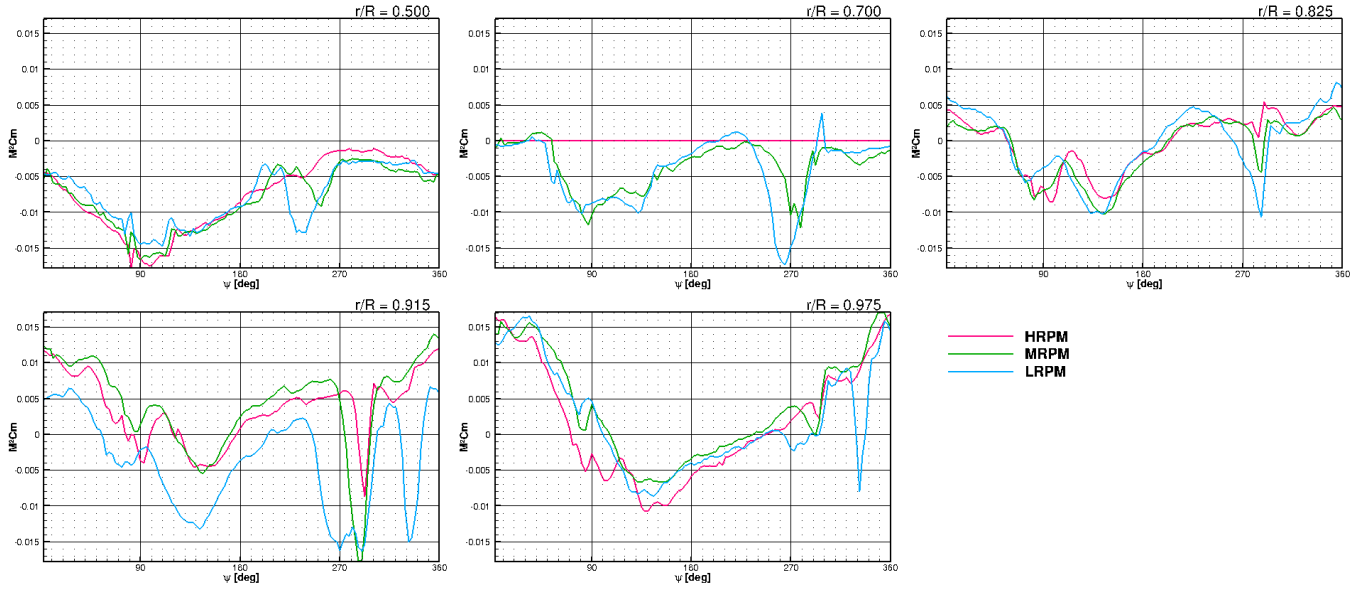

Fig. 3: Experimental sectional pitching moment coefficient M^2C_m.

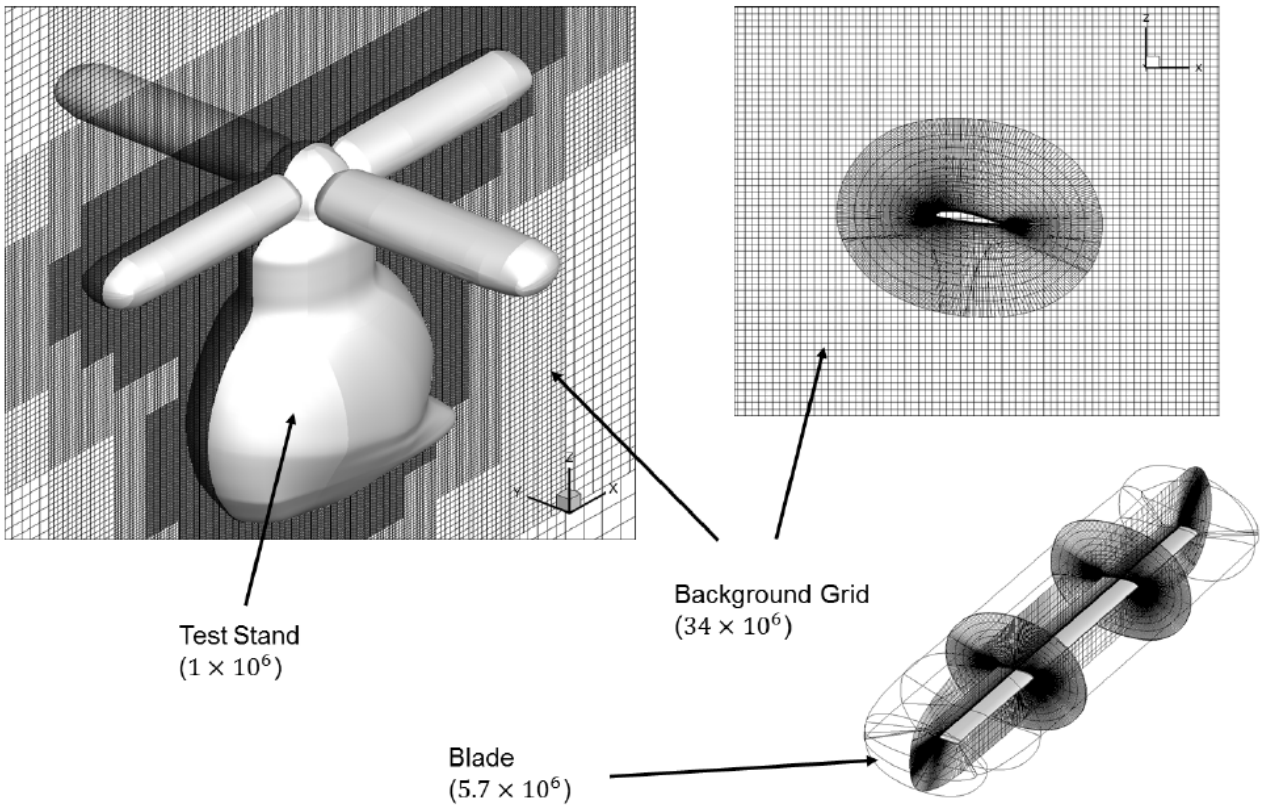

Fig. 4: Structured mesh: Chimera backgroung grid, blade mesh, rotor and test stand surface mesh.

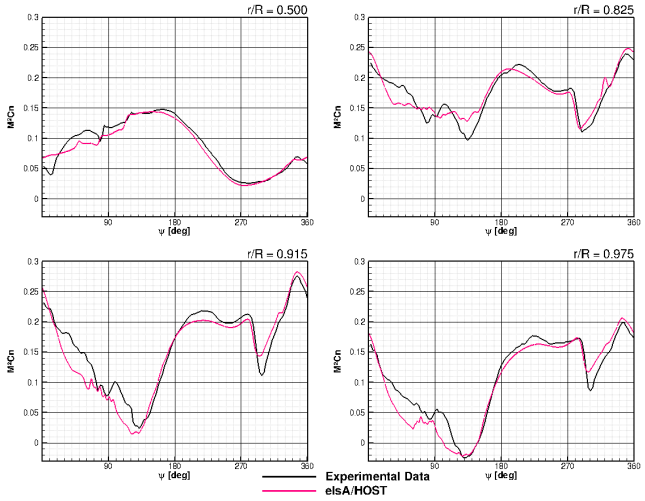

Fig. 5: Sectional normal force coefficient M^2C_n for the High RPM case.

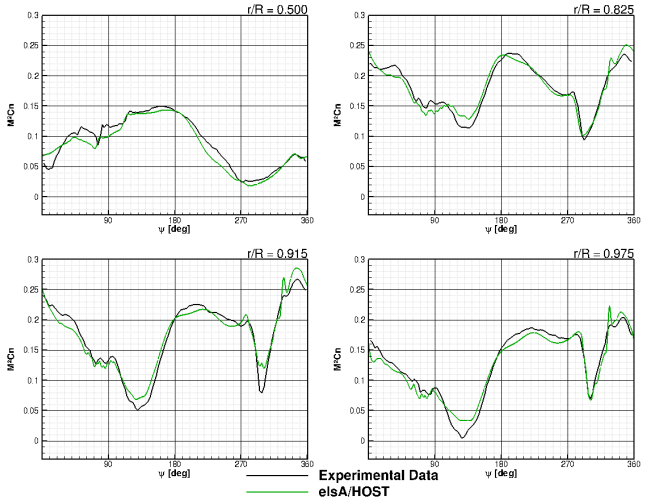

Fig. 6: Sectional normal force coefficient M^2C_n for the Moderate RPM case.

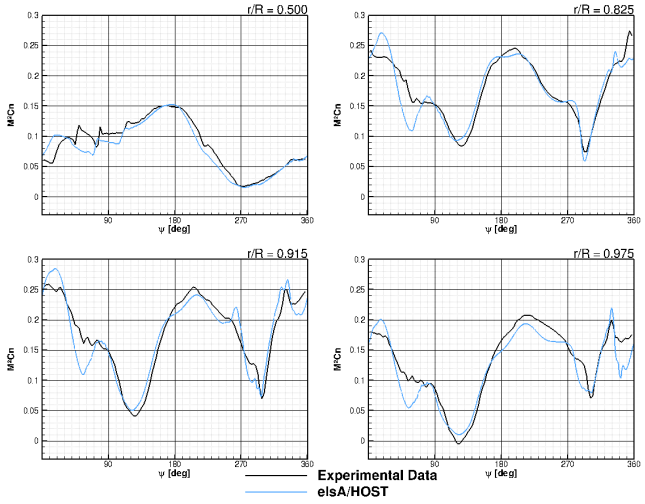

Fig. 7: Sectional normal force coefficient M^2C_n for the Low RPM Case.

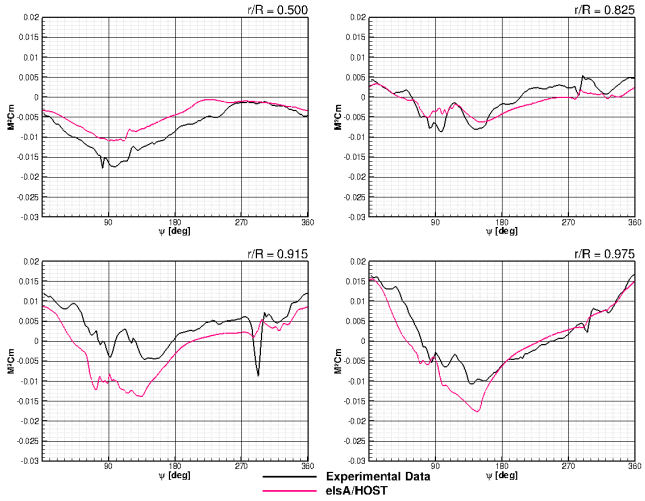

Fig. 8: Sectional pitching moment coefficient M^2C_m for the High RPM case.

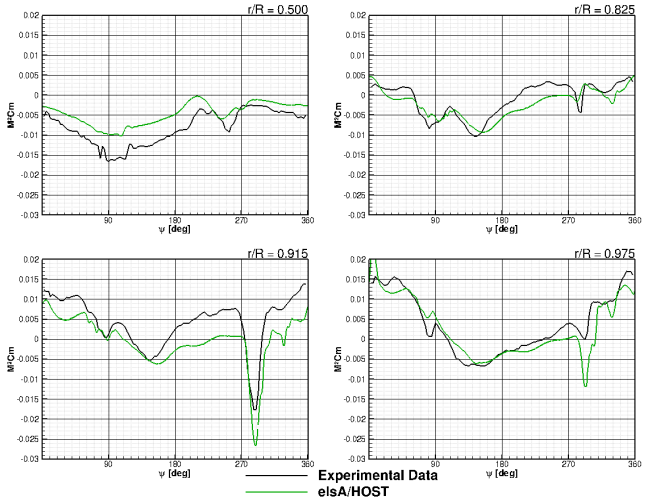

Fig. 9: Sectional pitching moment coefficient M^2C_m for the Moderate RPM case.

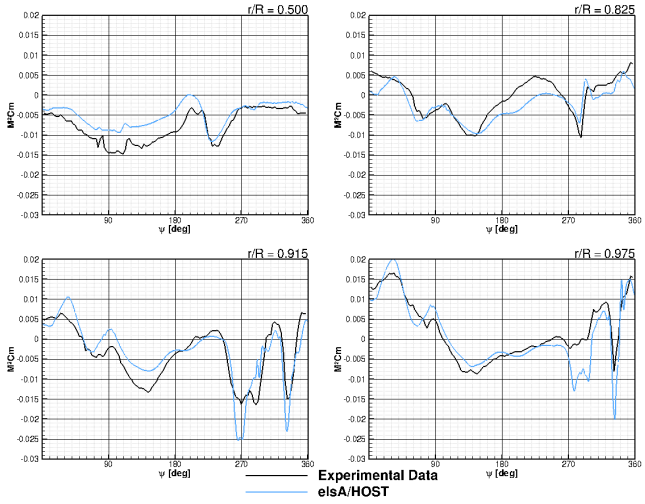

Fig. 10: Sectional pitching moment coefficient M^2C_m for the Low RPM Case.

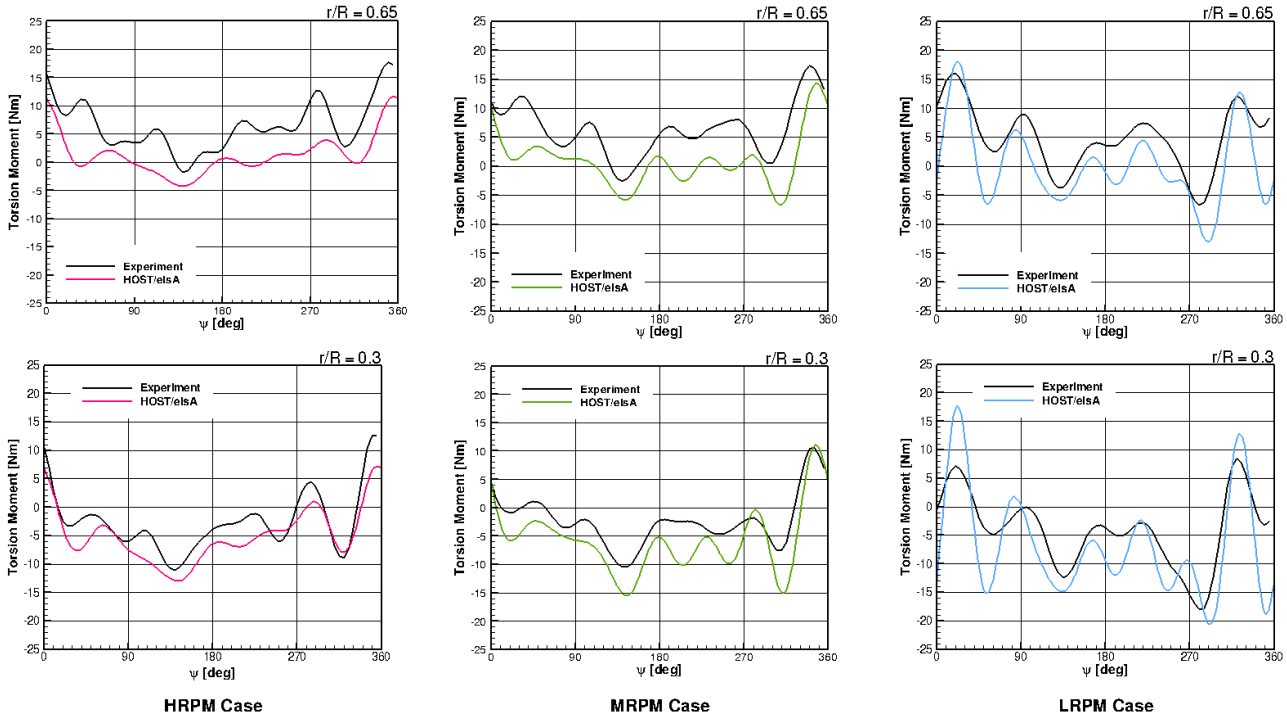

Fig. 11: Torsion Moment.

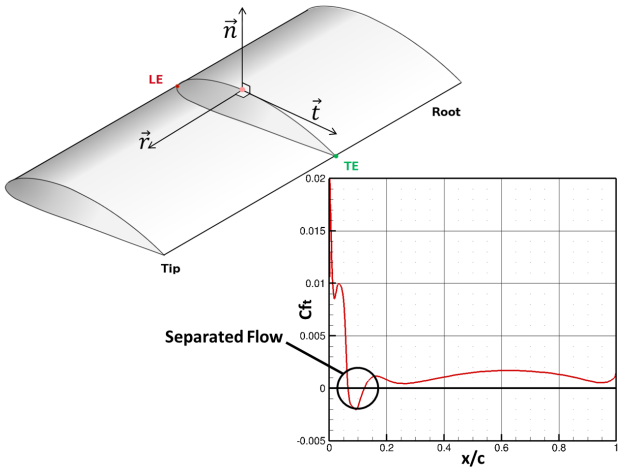

Fig. 12: Schematic representation of the method used for separated flow detection.

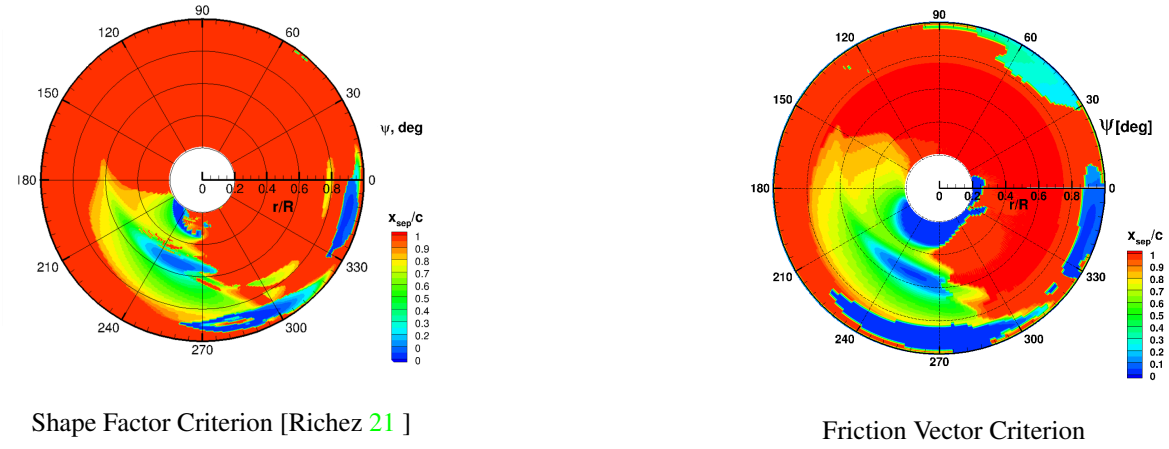

Shape Factor Criterion [Richez 21]

Friction Vector Criterion

Fig. 13: Rotormaps of the chordwise position of flow separation x_{sep}/c using two different citeria.

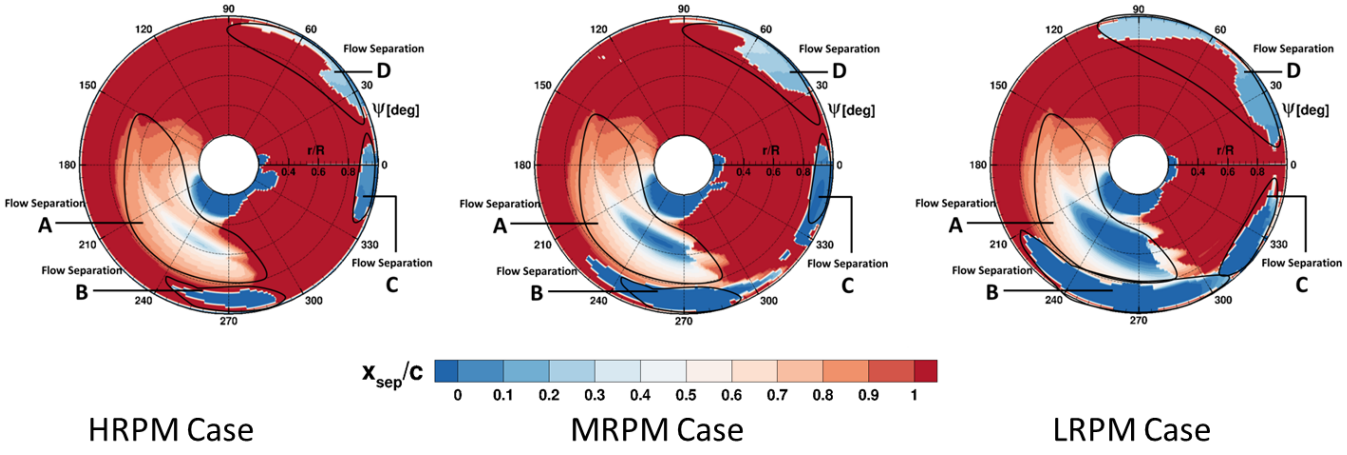

Fig. 14: Rotormaps of the chordwise position of flow separation x_{sep}/c. The black lines identify the flow separation regions.

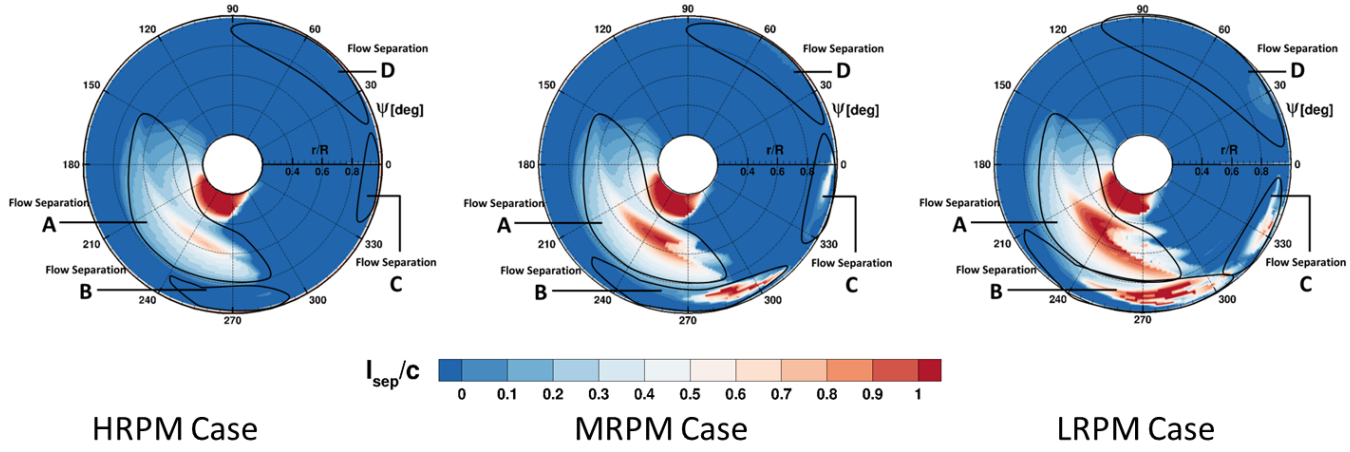

Fig. 15: Rotormaps of the chordwise length of flow separation l_{sep}/c.

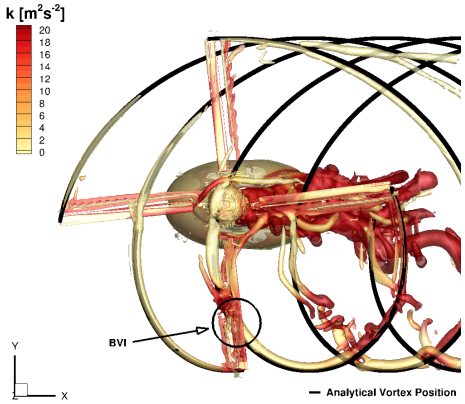

Fig. 16: Analytical tip vortex and isocontour of Q-criterion colored by the turbulent kinetic energy (MRPM).

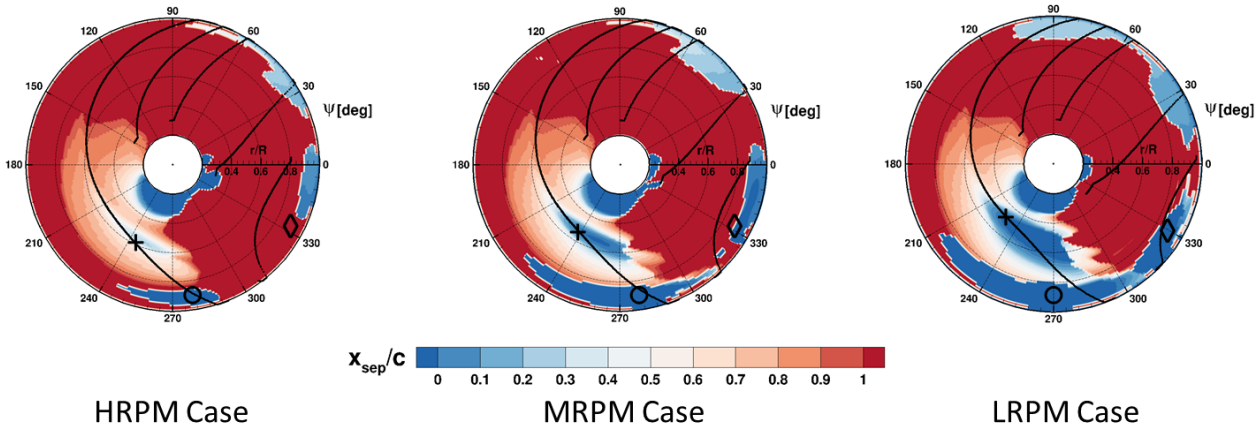

Fig. 17: Rotormaps of the chordwise position of flow separation x_{sep}/c. Black lines represent the analytical position of the blade-vortex interaction. $+$, $\circ$ and $\diamond$ correspond to the position of the maximum separation length respectively in region A, B and C.

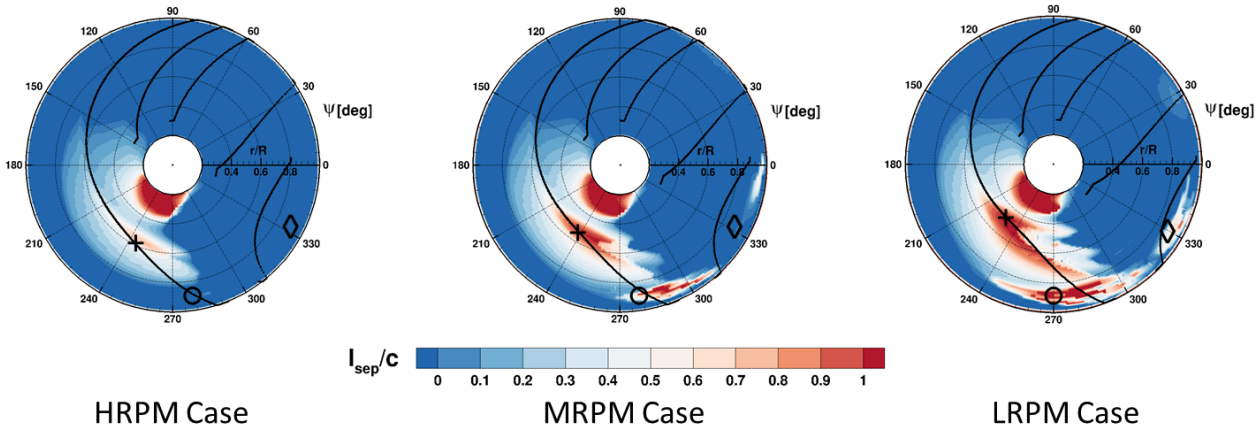

Fig. 18: Rotormaps of the chordwise length of flow separation l_{sep}/c. Black lines represent the analytical position of the blade-vortex interaction. $+$, $\circ$ and $\diamond$ correspond to the position of the maximum separation length respectively in region A, B and C.

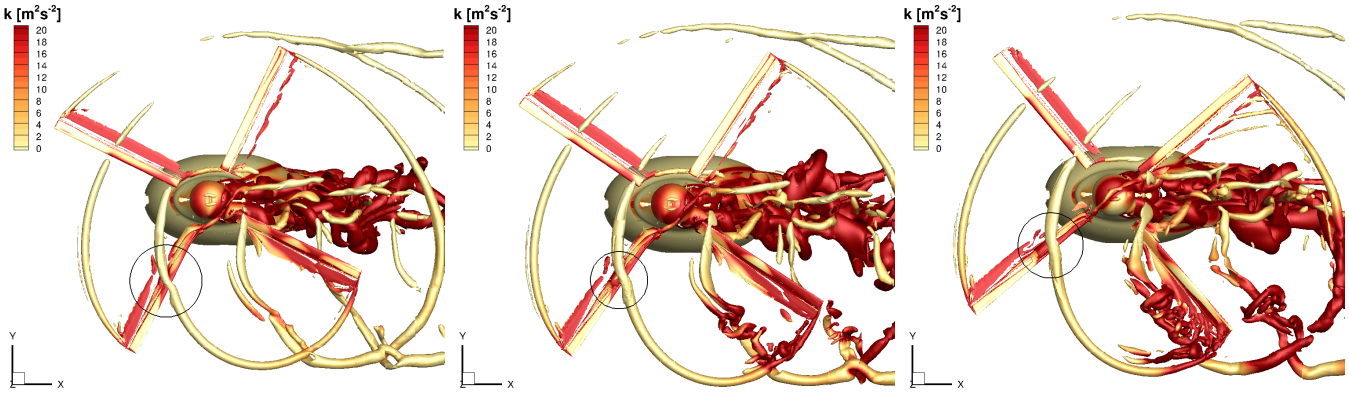

$\psi_{retreating\,blade} = 250\,\text{deg}$ (HRPM). $\psi_{retreating\,blade} = 240\,\text{deg}$ (MRPM). $\psi_{retreating\,blade} = 225\,\text{deg}$ (LRPM).

Fig. 19: Isocontour of Q criterion colored by the turbulent kinetic energy for the blade at the position marked by + in Fig 17-18.

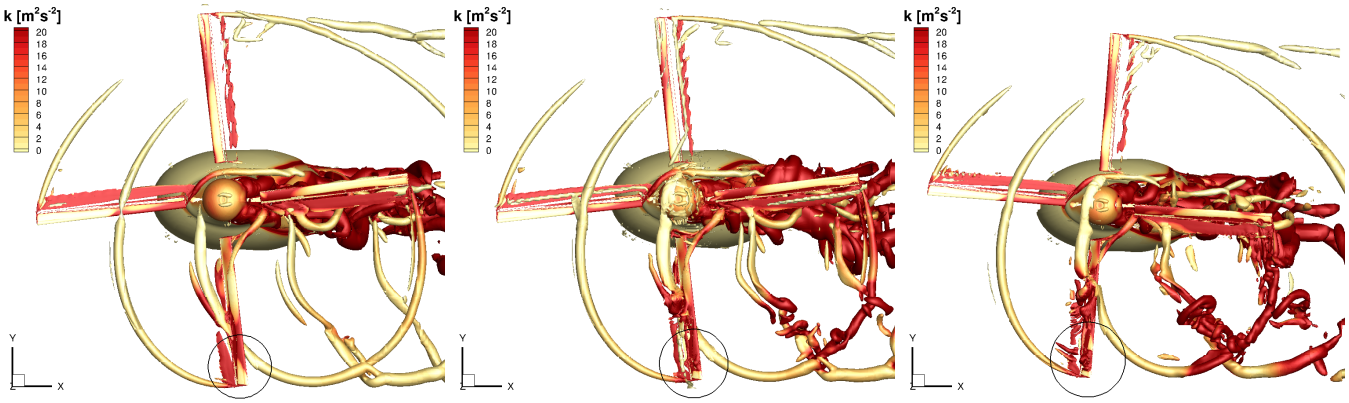

$\psi_{retreating\,blade} = 280\,\text{deg}$ (HRPM). $\psi_{retreating\,blade} = 280\,\text{deg}$ (MRPM). $\psi_{retreating\,blade} = 260\,\text{deg}$ (LRPM).

Fig. 20: Isocontour of Q criterion colored by the turbulent kinetic energy for the blade at the position marked by ○ in Fig 17-18.

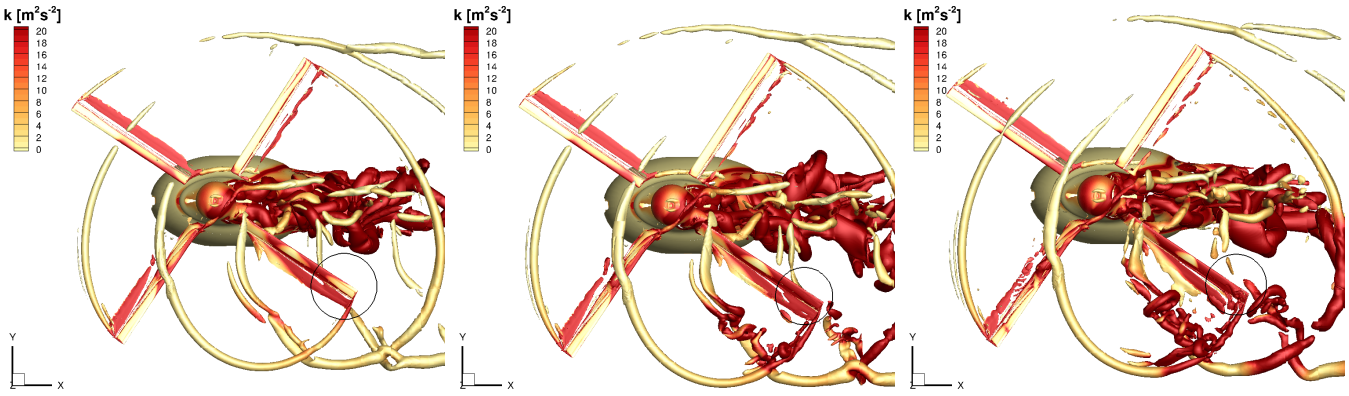

$\psi_{retreating\,blade} = 330\,\text{deg}$ (HRPM). $\psi_{retreating\,blade} = 330\,\text{deg}$ (MRPM). $\psi_{retreating\,blade} = 330\,\text{deg}$ (LRPM).

Fig. 21: Isocontour of Q criterion colored by the turbulent kinetic energy for the blade at the position marked by ◇ in Fig 17-18.

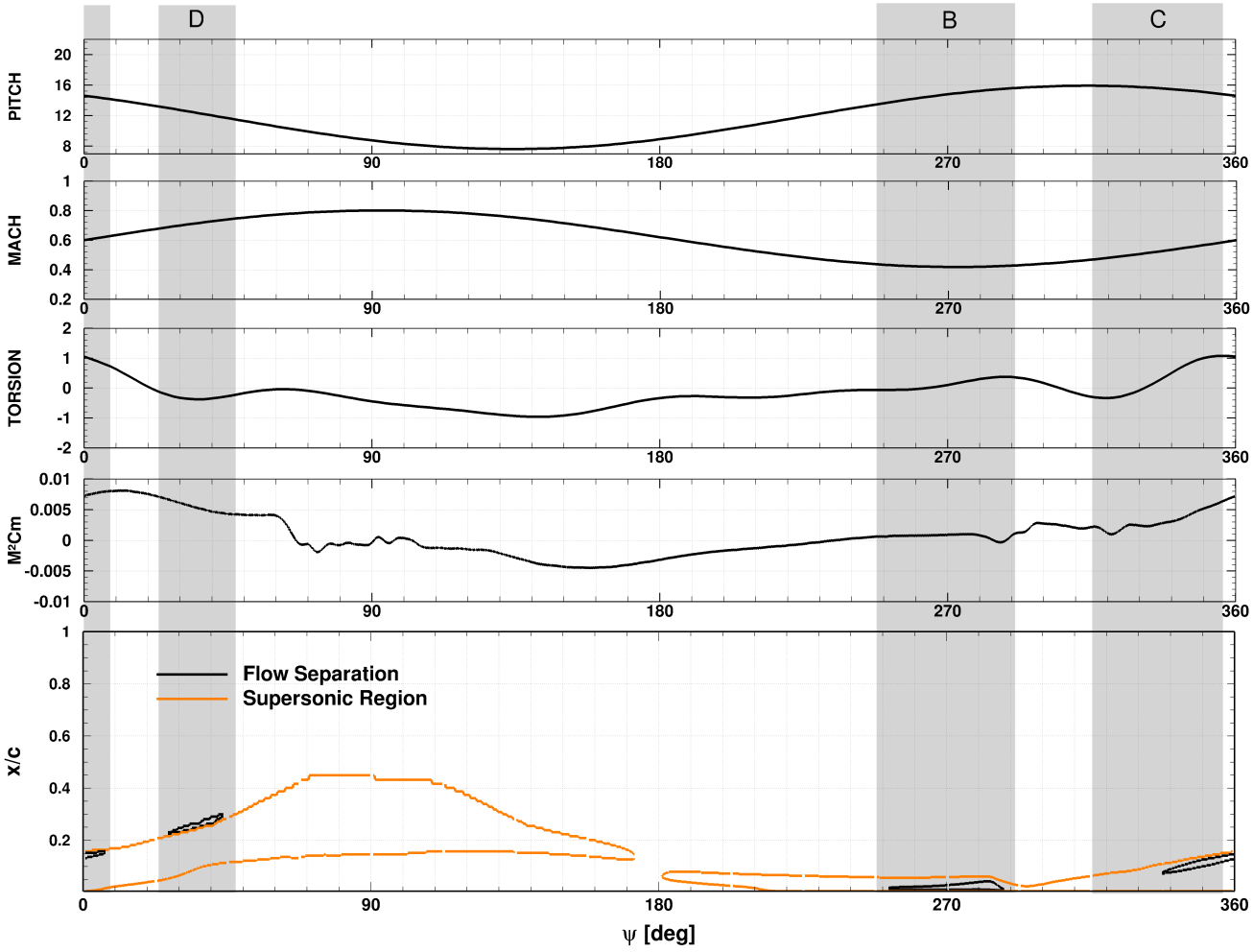

Fig. 22: Representation of the evolution of the Mach number, torsion angle, the pitching moment coefficient, the flow separation region and the chordwise position of the shock at $r/R = 0.915$ section (**HRPM**).

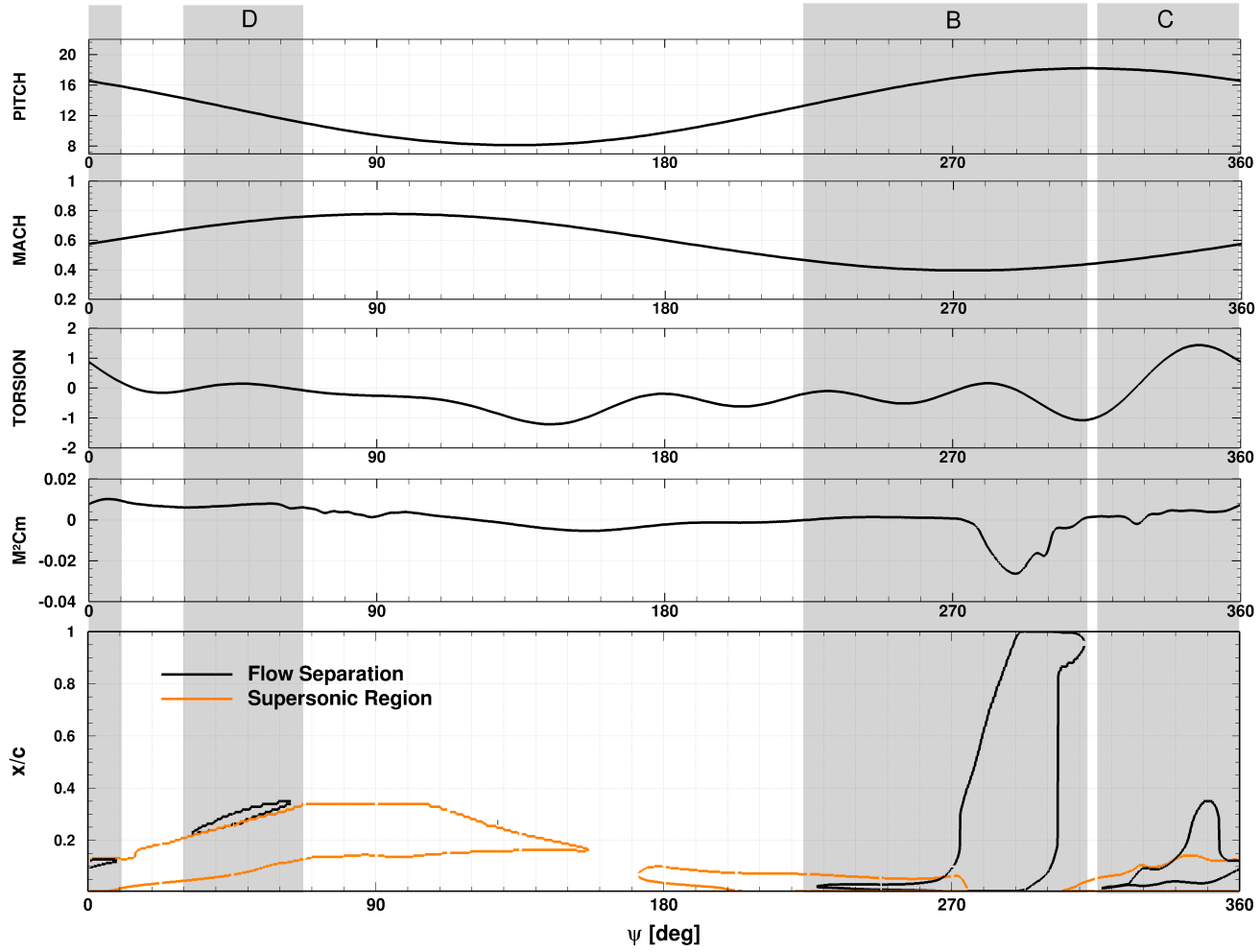

Fig. 23: Representation of the evolution of the Mach number, torsion angle, the pitching moment coefficient, the flow separation region and the chordwise position of the shock at $r/R = 0.915$ section (**MRPM**).

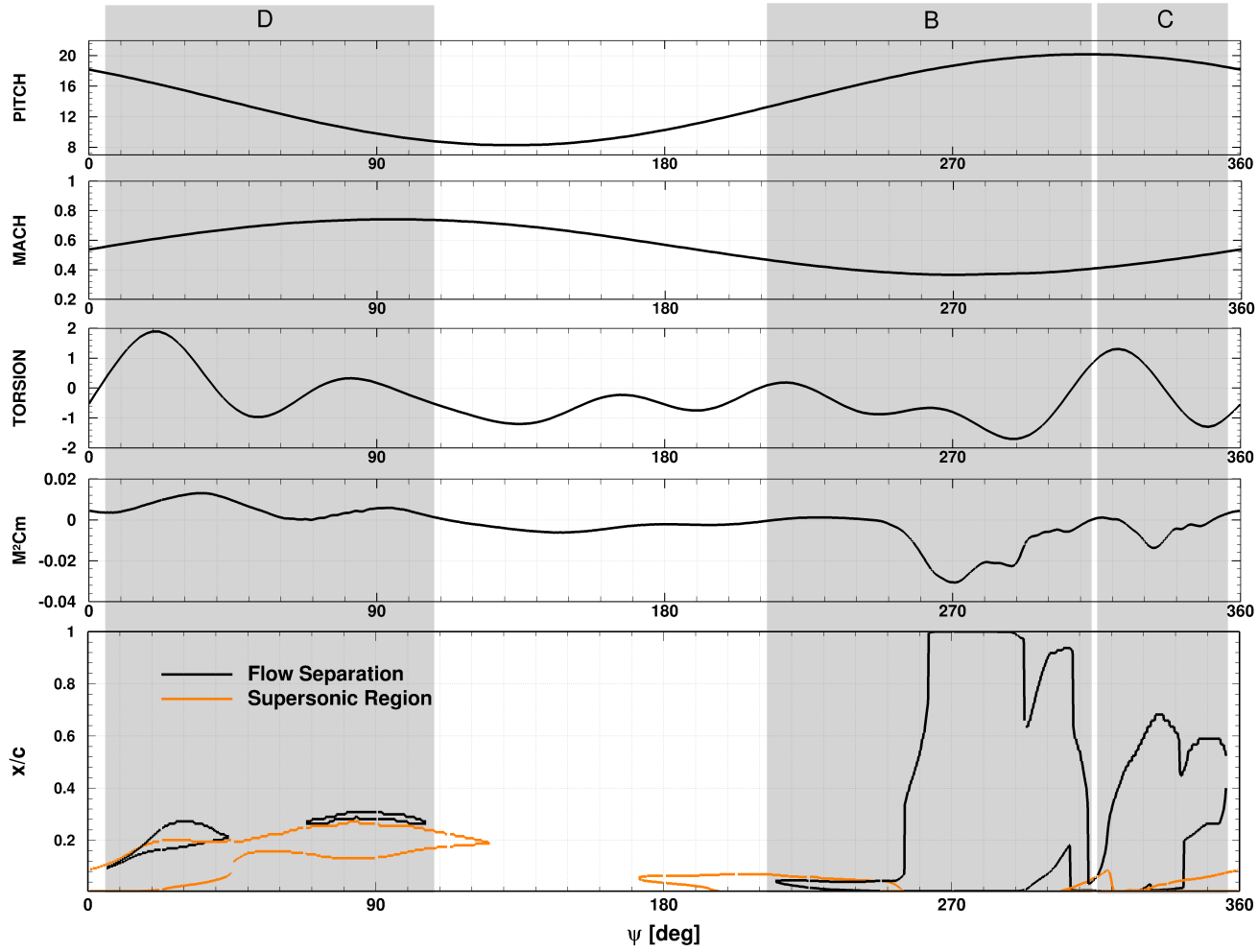

Fig. 24: Representation of the evolution of the Mach number, torsion angle, the pitching moment coefficient, the flow separation region and the chordwise position of the shock at $r/R = 0.915$ section (**LRPM**).